CHALMERS
UNIVERSITY OF TECHNOLOGY

Thermal Modeling of Battery Cells for Optimal Tab and Surface Cooling Control

Downloaded from: https://research.chalmers.se, 2026-09-08 03:49 UTC

Citation for the original published paper (version of record):
Peprah, G., Huang, Y., Wik, T. et al (2026). Thermal Modeling of Battery Cells for Optimal Tab and Surface Cooling Control. IEEE Transactions on Control Systems Technology, 34(4): 1831-1844.
http://dx.doi.org/10.1109/TCST.2026.3675726

N.B. When citing this work, cite the original published paper.

© 2026 IEEE. Personal use of this material is permitted. Permission from IEEE must be obtained for all other uses, in any current or future media, including reprinting/republishing this material for advertising or promotional purposes, or reuse of any copyrighted component of this work in other works.

(article starts on next page)

Thermal Modeling of Battery Cells for Optimal Tab and Surface Cooling Control

Godwin K. Peprah, *Student Member, IEEE*, Yicun Huang, Torsten Wik, *Member, IEEE*, Faisal Altaf, and Changfu Zou, *Senior Member, IEEE*

***Abstract*—Optimal cooling that minimizes thermal gradients and the average temperature is essential for enhanced battery safety and health. This work presents a new modeling approach for battery cells of different shapes by integrating the Chebyshev spectral-Galerkin (CSG) method and model component decomposition. As a result, a library of reduced-order, computationally efficient battery thermal models is obtained, characterized by different numbers of states. These models are validated against a high-fidelity finite-element model and are compared with a thermal equivalent circuit (TEC) model under real-world vehicle driving and battery cooling scenarios. Illustrative results demonstrate that the proposed model with four states can faithfully capture the 2-D thermal dynamics, while the model with only one state significantly outperforms the widely used two-state TEC model in both accuracy and computational efficiency, reducing computation time by 28.7%. Furthermore, our developed models allow for independent control of tab and surface cooling (SC) channels, enabling effective thermal performance optimization. Additionally, the proposed model's versatility and effectiveness are demonstrated through various applications, including the evaluation of different cooling scenarios, closed-loop temperature control, and the thermal assessment of cell aspect ratio.**

***Index Terms*—Battery management system (BMS), control-oriented thermal modeling, cooling control, spectral method, thermal management.**

I. Introduction

THE pursuit of carbon-neutral energy sources has emerged as a compelling and sustainable alternative to traditional nonrenewable energy such as fossil fuels. This shift has been driven by the growing global commitment to combat climate change through the reduction of carbon emissions, particularly in the transportation sector [1]. Central to achieving this cleaner and more efficient mobility solution is the adoption of electric vehicles (EVs), whose performance strongly depends on the battery pack performance. Temperature affects several aspects of the battery, including safety, electrochemical processes, charge acceptance, round-trip efficiency, power and energy capability, and lifetime [2]. This underscores the need for a sophisticated thermal management system [3] capable of controlling the battery temperature to desired values regardless of operating conditions.

Subject to various thermal boundary conditions such as liquid or air convection [4], battery cells can be thermally controlled at different interfaces, including the electrical connection tabs (terminals), selected regions of the external cell casing, or both [5]. Prior literature studies have investigated the impact of tab and lateral surface cooling (SC) methods on battery thermal performance. Hunt et al. [6] and Zhao et al. [7] concluded that lateral SC is more effective at maintaining lower average temperatures in lithium (Li)-ion pouch cells, especially under high current rates, due to the larger cooling area. In a case study, these authors also demonstrated that tab cooling extended the lifetime of a battery pack by a factor of three, primarily due to the more uniform temperature distribution it provides. In a follow-up study, Dondelewski et al. [8] compared both methods and found that SC resulted in lower average temperatures and slower degradation but reduced usable capacity. Conversely, tab cooling produced higher average temperatures and faster degradation, yet allowed for greater usable capacity due to more effective thermal distribution. Similar results were achieved for cylindrical Li-ion cells in [9] and [10], where tab cooling was shown to reduce internal temperature inhomogeneities by approximately 25%, though it resulted in a higher average cell temperature. Furthermore, Ahmad et al. [11] reported that SC causes a faster drop in temperature, driven by the larger lateral surface area available for heat transfer. However, tab cooling offered improved thermal uniformity, with a recorded temperature difference of 1.9 ° C, compared to 3.8 ° C under SC.

It is clear that both lateral surface and tab cooling offer distinct advantages; SC can enable faster heat removal and lower average cell temperatures, while tab cooling enhances temperature uniformity and thermal balance. However, to the best of our knowledge, there is currently no battery control framework in the state-of-the-art literature that systematically investigates the optimal integration of these two cooling methods for advanced battery thermal management.

Received 12 April 2025; revised 7 December 2025; accepted 8 March 2026. Date of publication 24 March 2026; date of current version 26 June 2026. This work was supported in part by the Swedish Electromobility Centre and Swedish Energy Agency under Grant 13011, in part by the Swedish Research Council under Grant 2019-04873, and in part by European Union's Horizon Europe Program through the Marie Skłodowska-Curie under Grant 101131278. Recommended by Associate Editor J. B. Siegel. *(Corresponding author: Changfu Zou.)*

Godwin K. Peprah, Torsten Wik, and Changfu Zou are with the Department of Electrical Engineering, Chalmers University of Technology, 41296 Gothenburg, Sweden (e-mail: godwinp@chalmers.se; tw@chalmers.se; changfu.zou@chalmers.se).

Yicun Huang was with the Department of Electrical Engineering, Chalmers University of Technology, 41296 Gothenburg, Sweden. He is now with the Department of Information Technology, Uppsala University, 75105 Uppsala, Sweden (e-mail: yicun.huang@it.uu.se).

Faisal Altaf was with the Department of Electromobility, Volvo Group, 40508 Gothenburg, Sweden. He is now with the Department of Energy Platform, Jaguar Land Rover, CV35 0BJ Warwick, U.K. (e-mail: faltaf2@jaguarlandrover.com).

Digital Object Identifier 10.1109/TCST.2026.3675726

© 2026 The Authors. This work is licensed under a Creative Commons Attribution 4.0 License.
For more information, see https://creativecommons.org/licenses/by/4.0/

Thermal equivalent circuit (TEC) models with lumped parameters have been extensively utilized for control-oriented modeling of batteries due to their ease of implementation and computational efficiency [12], [13]. However, TECs can only predict average and surface temperatures, and their applicability is limited to cells with small Biot numbers. Physics-based models [14] result in partial differential equations (PDEs) governing the underlying heat diffusion. They can predict the spatially distributed temperature field throughout the cell, but are typically implemented via computationally expensive numerical schemes, such as the finite-element method (FEM) and finite-difference method (FDM), rendering them impractical for real-time control purposes. Spectral methods [15], [16] are alternative numerical methods for finding solutions to PDEs. They belong to the class of weighted residual methods, and unlike FEM and FDM, they make use of global (rather than local) approximating functions in the discretization of the spatial domain, rendering them computationally efficient. With this benefit in mind, the spectral method based on the Galerkin approach was adopted to develop low-order 2-D thermal models for cylindrical cells in [17] and for pouch cells in [18]. However, these models do not allow independent and targeted cooling control of battery tabs and surfaces, preventing their use for optimally combining tab and SC for battery thermal management.

To bridge the identified research gap, we propose new 2D battery thermal models that stem from the decomposition of the particular solution of the nonhomogeneous PDE-based 2D heat equation. Unlike [17], [18], which used a lumped particular solution to capture all sides of the cell in one go, our model decomposes the particular solution into four components, each representing a distinct side of the battery cell. This method and its resulting model formulation enable us to obtain independent control signals for each side of the battery, including the tabs and surfaces.

For a given battery system and usage profile, the choice of the most suitable cooling scenario can significantly impact its key characteristics. Hence, we conduct a model-based analysis to study the performance tradeoffs amongst different cooling scenarios. Additionally, we demonstrate the application of the model to study thermal gradients under various C-rates, through a simple feedback temperature control strategy based on multiple proportional-integral (PI) controllers. Finally, using cylindrical cells as an example, we conduct a model-based study on the influence of varying dimensions on battery thermal performance.

The novel models can accurately predict the spatially resolved full temperature distribution throughout battery cells of any geometry (cylindrical, pouch, and prismatic) with higher computational efficiency compared to TEC models. Hence, it can be readily used for real-time optimal control in battery management systems (BMSs), particularly for the management of the cooling effort applied to battery tabs and surfaces. It can be an efficient simulation tool for understanding battery thermal dynamics to guide the design of next-generation cooling systems and battery cells.

The remainder of this article is organized as follows. Section II details the problem underlying the battery thermal modeling. Section III presents the proposed modeling framework for joint tab and SC control. Section IV presents the model validation and evaluation results. Section V showcases the efficacy of the model through various model-based applications and analyses. Finally, Section VI concludes the work.

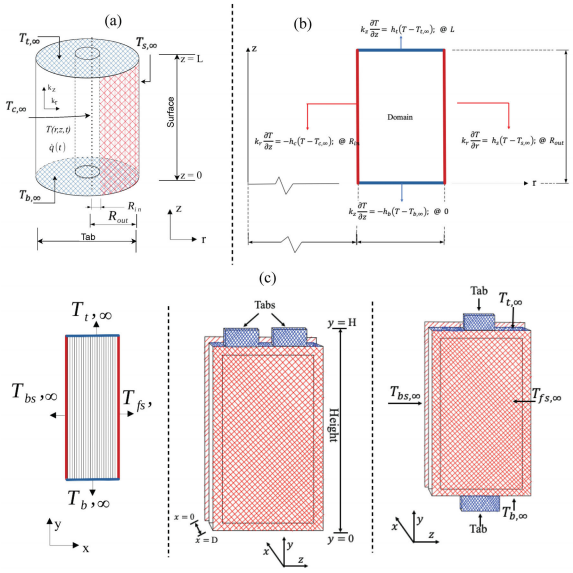

Fig. 1. Schematics of different shapes of battery cells for 2-D thermal modeling, with the blue- and red-shaded areas representing tab and SC channels, respectively. (a) Cylindrical cell cooled on the top and bottom tabs and part of the curved surface. (b) Illustration of the boundary conditions of (2) for cylindrical battery cell modeling. (c) Pouch cell whose tabs can either be on either the top, bottom, or both sides.

II. Overview of the PDE-Based Thermal Model

Battery cells of cylindrical and pouch types are widely used for electrical energy storage, as schematized in Figs. 1(a)–(c). Considering the symmetric structure along the radial (r) direction of a cylindrical cell, and by assuming the same thermal conductivity in y- and z-directions of a pouch cell, the temperature distribution of both cell types can be modeled in 2-D. For completeness, this section briefly reviews the first principle PDE-based models for battery thermal dynamics, including mathematical formulations as well as their underlying assumptions and considerations.

A. Cylindrical Cell Modeling

For the cylindrical cell, the governing equation for temperature $T(r,z,t)$ at time t and position (r,z) can be represented by the following 2-D boundary value problem [19]:

$$\rho c_p \frac{\partial T(r,z,t)}{\partial t} - k_r \frac{\partial^2 T(r,z,t)}{\partial r^2} - k_r \frac{\partial T(r,z,t)}{r\partial r} - k_z \frac{\partial^2 T(r,z,t)}{\partial z^2} = q(t) \tag{1}$$

subject to the nonhomogeneous convection Robin boundary conditions given by

$$k_r \frac{\partial T}{\partial r} = h_s \left(T - T_{s,\infty}\right) \quad \text{at } r = R_{\text{out}} \tag{2a}$$

$$k_r \frac{\partial T}{\partial r} = -h_c \left(T - T_{c,\infty}\right) \text{at } r = R_{\text{in}} \tag{2b}$$

$$k_z \frac{\partial T}{\partial z} = h_t \left(T - T_{t,\infty}\right) \quad \text{at } z = L \tag{2c}$$

$$k_z \frac{\partial T}{\partial z} = -h_b \left(T - T_{b,\infty}\right) \text{at } z = 0 \tag{2d}$$

where ρ, c_p, k, h, and T_∞ represent the volume-average density, volume-average specific heat capacity, thermal conductivity, convection coefficient, and fluid free-stream temperature, respectively. R_{in} and R_{out} are the cylindrical cell's inner and outer radius, and L is the length. The subscripts s, c, t, and b denote the cell's surface, core, top, and bottom, respectively. Equation (2) is illustrated in Fig. 1(b), where the convective heat transfer is presumed to occur on the external surfaces, and the heat transfer coefficient and fluid free-stream temperatures may differ for each surface. The cooling occurring in the core area is considered as zero, leading to the corresponding convection coefficient $h_c = 0$ in (2b).

The cylindrical cell's multilayer composition is considered a homogeneous solid with anisotropic thermal conductivities along r- and z-directions. Due to the spirally wound structure of the electrodes of the cylindrical cell, the thermal conductivity k_r would differ slightly from the inner to the outer radius, but is assumed constant in this study for simplicity. The heat generation rate $q(t)$ in (1) is assumed to be uniformly distributed in space.

For cylindrical cells, the tabs placed on the top and bottom sides can have different sizes. Existing designs make the tab's area much smaller than the cell's top/bottom area. It has been demonstrated that these designs of cylindrical cells are not efficient for battery cooling, merely from the tabs [9], [20], [21]. In this regard, this work considers the entire area of the top/bottom as the tab, forming the so-called all-tab or tab-less cell design, as illustrated in Fig. 1(a) and (b). Correspondingly, the thermal convection coefficients h_t and h_b in (2) are affected by the entire top and bottom areas, respectively, in addition to the applied cooling media.

B. Pouch Cell Modeling

The thermal model for pouch cells illustrated in Fig. 1(c) can be derived similarly as for the cylindrical cell. The thermal conductivity in the y-direction is assumed to be identical to that of the z-direction because of the stacked structure of the pouch cell. In addition, symmetric cooling is assumed along the thin side edges of the pouch cell (the z-direction boundaries). By treating the pouch cell's multilayer structure as a homogeneous solid with anisotropic thermal conductivities k_x in the x-direction and k_y in the y-direction, the governing heat equation in Cartesian coordinates is given by the 2-D boundary value problem [19]

$$\rho c_p \frac{\partial T(x,y,t)}{\partial t} - k_x \frac{\partial^2 T(x,y,t)}{\partial x^2} - k_y \frac{\partial^2 T(x,y,t)}{\partial y^2} = q(t) \tag{3}$$

subject to the nonhomogeneous convection Robin boundary conditions expressed as

$$k_x \frac{\partial T}{\partial x} = h_{fs} \left(T - T_{fs,\infty}\right) \quad \text{at } x = D \tag{4a}$$

$$k_x \frac{\partial T}{\partial x} = -h_{bs} \left(T - T_{bs,\infty}\right) \text{at } x = 0 \tag{4b}$$

$$k_y \frac{\partial T}{\partial y} = h_t \left(T - T_{t,\infty}\right) \quad \text{at } y = H \tag{4c}$$

$$k_y \frac{\partial T}{\partial y} = -h_b \left(T - T_{b,\infty}\right) \quad \text{at } y = 0 \tag{4d}$$

where D, H, the subscripts fs, and bs represent the pouch cell's width, height, front side, and back side, respectively.

III. Control-Oriented Battery Thermal Modeling

In this section, we demonstrate the control-oriented modeling process for the thermal behavior of cylindrical cells. The model for pouch cells, which can be derived similarly, is introduced briefly afterward.

A. Model Nondimensionalization

To facilitate model approximation, reduction, and the subsequent analyses, we first remove all physical dimensions involved in the model's governing (1). Specifically, new coordinate variables are introduced along the radius and height directions

$$\tilde{r} = \alpha r - \frac{R_{\text{out}} + R_{\text{in}}}{R_{\text{out}} - R_{\text{in}}} \tag{5a}$$

$$\tilde{z} = \beta z - 1 \tag{5b}$$

where $\alpha = 2/(R_{\text{out}} - R_{\text{in}})$ and $\beta = 2/L$. As a result, both $\tilde{r}$ and $\tilde{z}$ fall in the range of $[-1, 1]$. Replacing all r and z by $\tilde{r}$ and $\tilde{z}$, respectively, the initial 2-D thermal model for cylindrical cells is scaled and becomes

$$\rho c_p \frac{\partial T(\tilde{r},\tilde{z},t)}{\partial t} - \alpha^2 k_r \frac{\partial^2 T(\tilde{r},\tilde{z},t)}{\partial \tilde{r}^2} - \gamma \frac{\partial T(\tilde{r},\tilde{z},t)}{\partial \tilde{r}} - \beta^2 k_z \frac{\partial^2 T(\tilde{r},\tilde{z},t)}{\partial \tilde{z}^2} = q(t) \tag{6}$$

subject to the boundary conditions

$$h_s T - \alpha k_r \frac{\partial T}{\partial \tilde{r}} = u_s \quad \text{at } \tilde{r} = 1 \tag{7a}$$

$$-h_c T - \alpha k_r \frac{\partial T}{\partial \tilde{r}} = u_c \quad \text{at } \tilde{r} = -1 \tag{7b}$$

$$h_t T - \beta k_z \frac{\partial T}{\partial \tilde{z}} = u_t \quad \text{at } \tilde{z} = 1 \tag{7c}$$

$$-h_b T - \beta k_z \frac{\partial T}{\partial \tilde{z}} = u_b \quad \text{at } \tilde{z} = -1 \tag{7d}$$

with $\gamma = \alpha^2 k_r/(1 + \tilde{r} + \alpha R_{\text{in}})$. The cooling power applied per unit area is denoted by u, and its values at the different sides of the cell are given, respectively, by

$$u_s(t) = h_s(t) T_{s,\infty}(t), \quad u_c(t) = -h_c(t) T_{c,\infty}(t) = 0 \tag{8a}$$

$$u_t(t) = h_t(t) T_{t,\infty}(t), \quad u_b(t) = -h_b(t) T_{b,\infty}(t). \tag{8b}$$

The above cooling power can be considered as the dynamic thermal system's input. The coolant's temperature and flow rate can influence each of these inputs. Furthermore, (8) can be integrated with a flow model to better capture the convective cooling effects and dynamic interactions between the coolant and the battery system under various cooling scenarios.

B. Overall Solution

According to the boundary lifting principle [16], [22], [23], the overall solution to the boundary value problem formulated in (6)–(8) is composed of the homogeneous solution T_h and the particular solution T_p. Namely, there exists

$$T(\tilde{r},\tilde{z},t) = T_h(\tilde{r},\tilde{z},t) + T_p(\tilde{r},\tilde{z},t). \tag{9}$$

Here, T_h satisfies the modified problem for the cylindrical cell with the governing equation

$$\rho c_p \frac{\partial T_h}{\partial t} - \alpha^2 k_r \frac{\partial^2 T_h}{\partial \tilde{r}^2} - \gamma \frac{\partial T_h}{\partial \tilde{r}} - \beta^2 k_z \frac{\partial^2 T_h}{\partial \tilde{z}^2} = q^* \tag{10}$$

and the homogeneous boundary conditions

$$h_s T_h - \alpha k_r \frac{\partial T_h}{\partial \tilde{r}} = 0 \qquad \text{at } \tilde{r} = 1 \tag{11a}$$

$$-h_c T_h - \alpha k_r \frac{\partial T_h}{\partial \tilde{r}} = 0 \qquad \text{at } \tilde{r} = -1 \tag{11b}$$

$$h_t T_h - \beta k_z \frac{\partial T_h}{\partial \tilde{z}} = 0 \qquad \text{at } \tilde{z} = 1 \tag{11c}$$

$$-h_b T_h - \beta k_z \frac{\partial T_h}{\partial \tilde{z}} = 0 \qquad \text{at } \tilde{z} = -1 \tag{11d}$$

where q^* in (10) is defined as

$$q^* \triangleq q - \left(-\alpha^2 k_r \frac{\partial^2 T_p}{\partial \tilde{r}^2} - \gamma \frac{\partial T_p}{\partial \tilde{r}} - \beta^2 k_z \frac{\partial^2 T_p}{\partial \tilde{z}^2}\right). \tag{12}$$

The particular solution for the locally distributed temperature T_p in (9) satisfies the original boundary conditions defined in (7), leading to

$$h_s T_p - \alpha k_r \frac{\partial T_p}{\partial \tilde{r}} = u_s \qquad \text{at } \tilde{r} = 1 \tag{13a}$$

$$-h_c T_p - \alpha k_r \frac{\partial T_p}{\partial \tilde{r}} = u_c \qquad \text{at } \tilde{r} = -1 \tag{13b}$$

$$h_t T_p - \beta k_z \frac{\partial T_p}{\partial \tilde{z}} = u_t \qquad \text{at } \tilde{z} = 1 \tag{13c}$$

$$-h_b T_p - \beta k_z \frac{\partial T_p}{\partial \tilde{z}} = u_b \qquad \text{at } \tilde{z} = -1. \tag{13d}$$

After the particular solution T_p is solved from (13), it can be substituted into (12) to facilitate the determination of the homogeneous solution T_h governed by (10)–(12).

C. Model Reduction for the Homogeneous Solution

The homogeneous problem given by (10)–(12) can be solved using the Chebyshev spectral-Galerkin (CSG) method. Although Jacobi's polynomials, such as Legendre or Chebyshev polynomials, could be effective candidates, Chebyshev functions are employed in this work because they can be readily defined to satisfy a wide range of boundary conditions [15], including the Robin boundary conditions encountered in this homogeneous problem.

Within the CSG method, the homogeneous solution T_h to the 2-D thermal model of cylindrical battery cells can be approximated by a finite sum of basis functions in the form of

$$\hat{T}_h(\tilde{r},\tilde{z},t) = \sum_{m=0}^{M}\sum_{n=0}^{N} c_{mn}(t)\,\phi_m^{\tilde{r}}(\tilde{r})\,\phi_n^{\tilde{z}}(\tilde{z}) \tag{14}$$

where $c_{mn}(t)$ are unknown expansion (solution) coefficients. $\phi_m^{\tilde{r}}(\tilde{r})$ is the mth Chebyshev basis function along the dimension $\tilde{r}$, satisfying the boundary conditions (11a) and (11b). M is the number of Chebyshev basis functions, and $m \in \{0,\ldots,M\}$. Along the dimension $\tilde{z}$, $\phi_n^{\tilde{z}}(\tilde{z})$ is the nth Chebyshev basis function satisfying the boundary conditions (11c) and (11d), where $n \in \{0,\ldots,N\}$. M and N are tuning parameters depending on the required accuracy.

Let $P_m(\tilde{r}) = \cos(m\theta^{\tilde{r}})$ and $P_n(\tilde{z}) = \cos(n\theta^{\tilde{z}})$, with $\theta^{\tilde{r}} = \arccos(\tilde{r})$ and $\theta^{\tilde{z}} = \arccos(\tilde{z})$. Here, $P_m(\tilde{r})$ and $P_n(\tilde{z})$ represent the Chebyshev polynomials of the first kind, of degrees m and n, respectively. In spectral methods, to enable efficient solution computations and satisfaction of boundary conditions, neighboring orthogonal polynomials should be used to form the basis functions. Therefore, we seek the basis functions as a compact combination of Chebyshev polynomials in the form [15]

$$\phi_m^{\tilde{r}}(\tilde{r}) = P_m(\tilde{r}) + a_m^{\tilde{r}}(\tilde{r})\,P_{m+1}(\tilde{r}) + b_m^{\tilde{r}}(\tilde{r})\,P_{m+2}(\tilde{r}) \tag{15a}$$

$$\phi_n^{\tilde{z}}(\tilde{z}) = P_n(\tilde{z}) + a_n^{\tilde{z}}(\tilde{z})\,P_{n+1}(\tilde{z}) + b_n^{\tilde{z}}(\tilde{z})\,P_{n+2}(\tilde{z}) \tag{15b}$$

where the coefficients $a_m^{\tilde{r}}$, $b_m^{\tilde{r}}$, $a_n^{\tilde{z}}$, and $b_n^{\tilde{z}}$ are defined according to [15 Lemma 4.3].

Substituting (14) for T_h into (10) yields the residual denoted by R

$$R = \rho c_p \frac{\partial \hat{T}_h}{\partial t} - \alpha^2 k_r \frac{\partial^2 \hat{T}_h}{\partial \tilde{r}^2} - \gamma \frac{\partial \hat{T}_h}{\partial \tilde{r}} - \beta^2 k_z \frac{\partial^2 \hat{T}_h}{\partial \tilde{z}^2} - q^* \neq 0. \tag{16}$$

The principle of the CSG method is to force the integral of the resulting residual R to zero as

$$\langle rR,\eta\rangle = \left\langle r\left[\rho c_p \frac{\partial \hat{T}_h}{\partial t} - \alpha^2 k_r \frac{\partial^2 \hat{T}_h}{\partial \tilde{r}^2} - \gamma \frac{\partial \hat{T}_h}{\partial \tilde{r}} - \beta^2 k_z \frac{\partial^2 \hat{T}_h}{\partial \tilde{z}^2} - q^*\right],\eta\right\rangle = 0 \tag{17}$$

where we use the notation $\langle f,\eta\rangle$ to represent the inner product of f and a test function η in the domain of $\tilde{r}$ and $\tilde{z}$, namely $\langle f,\eta\rangle = \int_{-1}^{1}\int_{-1}^{1} f(\tilde{r},\tilde{z})\eta(\tilde{r},\tilde{z})d\tilde{r}d\tilde{z}$. Note that r is included in (17) to account for cylindrical coordinates. For the CSG method, the test function η must belong to the same set of Chebyshev basis functions, thereby giving $\eta = \phi_m^{\tilde{r}}\phi_n^{\tilde{z}}$.

Substituting $\hat{T}_h$ in (17) with its actual form in (14), we have

$$\left\langle r\left[\rho c_p \frac{\partial\left(\sum_{m=0}^{M}\sum_{n=0}^{N} c_{mn}(t)\,\phi_m^{\tilde{r}}\phi_n^{\tilde{z}}\right)}{\partial t} - \alpha^2 k_r \frac{\partial^2\left(\sum_{m=0}^{M}\sum_{n=0}^{N} c_{mn}(t)\,\phi_m^{\tilde{r}}\phi_n^{\tilde{z}}\right)}{\partial \tilde{r}^2} - \gamma \frac{\partial\left(\sum_{m=0}^{M}\sum_{n=0}^{N} c_{mn}(t)\,\phi_m^{\tilde{r}}\phi_n^{\tilde{z}}\right)}{\partial \tilde{r}} - \beta^2 k_z \frac{\partial^2\left(\sum_{m=0}^{M}\sum_{n=0}^{N} c_{mn}(t)\,\phi_m^{\tilde{r}}\phi_n^{\tilde{z}}\right)}{\partial \tilde{z}^2} - q^*\right],\eta\right\rangle = 0. \tag{18}$$

Finally, rewriting (18) in matrix–vector notations, this gives (19), as shown at the bottom of the next page.

D. Model Reduction for the Particular Solution

Remark 1: Unlike the homogeneous solution, which often exhibits smoother spatial variations governed by the battery system's intrinsic properties, the particular solution T_p may require a more flexible representation to accommodate abrupt changes or spatial gradients induced by external factors such as boundary conditions. Additionally, T_p must satisfy not only the PDE (6) but also the nonhomogeneous boundary conditions (7) and any forcing terms, such as the heat generation q, presented in the problem. These additional constraints necessitate a richer and more flexible approach than a straightforward finite-sum expansion as employed in the homogeneous case.

Based on Remark 1, we develop a highly adaptable approach for solving the particular solution T_p. This approach will be able to effectively handle abrupt changes and spatial gradients while satisfying all constraints imposed by (6) and (7).

1) Approximation of T_p From a Polynomial Vector Space: As the first step of model reduction for the particular solution T_p, we project and approximate it from a polynomial vector space denoted by $\mathcal{V}_{rz}$. Following a similar approach as in [24] and [25], $\mathcal{V}_{rz}$ is defined as

$$\begin{aligned}\mathcal{V}_{rz} = &\left[\left\{\phi_m^{\tilde{r}}(\tilde{r}), 1 \le m \le M\right\} \otimes \left\{\tilde{z}, \tilde{z}^2\right\}\right] \\ &\oplus \left[\left\{\phi_n^{\tilde{z}}(\tilde{z}), 1 \le n \le N\right\} \otimes \left\{\tilde{r}, \tilde{r}^2\right\}\right]\end{aligned} \tag{20}$$

where $\otimes$ and $\oplus$ are the outer product and direct sum, respectively. $\tilde{z}$, $\tilde{z}^2$, $\tilde{r}$, and $\tilde{r}^2$ are the basis vectors of $\mathcal{V}_{rz}$. Equation (20) explicitly couples the $\tilde{r}$- and $\tilde{z}$-dimensions by combining basis functions from one dimension with polynomials in the other. This coupling is essential because the heat generation and boundary conditions can create interactions between $\tilde{r}$ and $\tilde{z}$ that a simpler product space might not capture effectively.

To elucidate the idea of finite-sum approximation in the vector space $\mathcal{V}_{rz}$, we start with a simple case. Consider a vector space $\mathcal{V}_y$ consisting of the basis vectors y and y^2. This space can be written as

$$\mathcal{V}_y = \text{span}\left\{y, y^2\right\}. \tag{21}$$

Any function, $f(y) \in \mathcal{V}_y$, can be represented as a linear combination of these basis vectors. Specifically, we can write any such $f(y)$ using a finite-sum approximation

$$f(y) \approx \sum_{i=0}^{2} p_i y^i \tag{22}$$

where p_i are the unknown coefficients, which can be determined using various methods, such as the least-squares or spectral methods.

Following the idea of finite-sum approximation introduced in (21) and (22), approximating T_p in the vector space $\mathcal{V}_{rz}$, that is, in two space dimensions, leads to the expansion

$$\begin{aligned}\hat{T}_p(\tilde{r}, \tilde{z}, t) = &\sum_{n=0}^{N} \left(D_{1,n}(\tilde{z}, t)\,\tilde{r} + D_{2,n}(\tilde{z}, t)\,\tilde{r}^2\right)\phi_n^{\tilde{z}}(\tilde{z}) \\ &+ \sum_{m=0}^{M} \left(D_{3,m}(\tilde{r}, t)\,\tilde{z} + D_{4,m}(\tilde{r}, t)\,\tilde{z}^2\right)\phi_m^{\tilde{r}}(\tilde{r})\end{aligned} \tag{23}$$

where $\hat{T}_p$ is the approximate solution of T_p, and $D_{1,n}, D_{2,n}, D_{3,m}$, and $D_{4,m}$ are unknown expansion coefficients. The first and second terms on the right-hand side of (23) represent the lumped particular solutions in the vertical and horizontal directions of the battery cell, respectively.

Remark 2: The deviation between $\hat{T}_p$ and T_p can arise from two primary sources: the chosen vector space along $\tilde{z}$ and $\tilde{r}$, and the finite-sum approximation, which depends on the tuning parameters N and M. Generally, using higher-order polynomials and including more terms in the finite sum results in smaller approximation errors but increases the number of expansion coefficients that need to be determined. The tradeoffs involved, as well as the applicability of this approximation method, will be quantitatively investigated in Section IV.

2) Determination of the Expansion Coefficients: Taking advantage of the orthogonality and approximation properties of the Chebyshev polynomials in (15), we employ the CSG method to solve for the boundary conditions formulated in (13). The process is similar to that for the homogeneous problem, with the details given in the following. Substituting (23) into the boundary condition at the surface side (13a), yields the residual R_s given by

$$R_s = h_s \hat{T}_p - \alpha k_r \frac{\partial \hat{T}_p}{\partial \tilde{r}} - u_s \neq 0, \quad \text{at } \tilde{r} = 1. \tag{24}$$

As the CSG method demands, we force the integral of the resulting residual R_s to zero as

$$\langle R_s, \phi_i^{\tilde{z}} \rangle_{\tilde{z}} = \left\langle \left[h_s \hat{T}_p - \alpha k_r \frac{\partial \hat{T}_p}{\partial \tilde{r}} - u_s \right], \phi_i^{\tilde{z}} \right\rangle_{\tilde{z}} = 0, \quad \text{at } \tilde{r} = 1 \tag{25}$$

where the notation $\langle f, \phi_i^{\tilde{z}} \rangle_{\tilde{z}} = \int_{-1}^{1} f(\tilde{z}) \phi_i^{\tilde{z}}(\tilde{z}) d\tilde{z}$ represents the 1-D inner product in the $\tilde{z}$-direction, and $\phi_i^{\tilde{z}}$ with $i \in \{0, \ldots, N\}$, are the test functions. Substituting $\hat{T}_p$ in (25) with its actual form in (23), and with $\tilde{r} = 1$, simplifies to

$$\begin{aligned}&\sum_{n=0}^{N} \left[D_{1,n}(h_s - \alpha k_r) + D_{2,n}(h_s - 2\alpha k_r)\right] \left\langle \phi_n^{\tilde{z}}, \phi_i^{\tilde{z}} \right\rangle_{\tilde{z}} \\ &= \left\langle u_s, \phi_i^{\tilde{z}} \right\rangle_{\tilde{z}}.\end{aligned} \tag{26}$$

$$\begin{aligned}\Bigg\langle r\Big[\rho c_p \left[\phi_1^{\tilde{r}}\phi_1^{\tilde{z}}, \cdots, \phi_M^{\tilde{r}}\phi_N^{\tilde{z}}\right] \begin{bmatrix} \dot{c}_{11}(t) \\ \vdots \\ \dot{c}_{MN}(t) \end{bmatrix} - \alpha^2 k_r \left[\frac{\partial^2 \phi_1^{\tilde{r}}\phi_1^{\tilde{z}}}{\partial \tilde{r}^2}, \cdots, \frac{\partial^2 \phi_M^{\tilde{r}}\phi_N^{\tilde{z}}}{\partial \tilde{r}^2}\right] \begin{bmatrix} c_{11}(t) \\ \vdots \\ c_{MN}(t) \end{bmatrix} \\ -\gamma \left[\frac{\partial \phi_1^{\tilde{r}}\phi_1^{\tilde{z}}}{\partial \tilde{r}}, \ldots, \frac{\partial \phi_M^{\tilde{r}}\phi_N^{\tilde{z}}}{\partial \tilde{r}}\right] \begin{bmatrix} c_{11}(t) \\ \vdots \\ c_{MN}(t) \end{bmatrix} - \beta^2 k_z \left[\frac{\partial^2 \phi_1^{\tilde{r}}\phi_1^{\tilde{z}}}{\partial \tilde{z}^2}, \ldots, \frac{\partial^2 \phi_M^{\tilde{r}}\phi_N^{\tilde{z}}}{\partial \tilde{z}^2}\right] \begin{bmatrix} c_{11}(t) \\ \vdots \\ c_{MN}(t) \end{bmatrix} - q^* \Bigg], \eta \Bigg\rangle = 0.\end{aligned} \tag{19}$$

Then, we adopt a similar process for the other vertical side (i.e., the core) and the horizontal sides (i.e., the top and bottom sides) of the battery cell with the boundary conditions formulated in (13b)–(13d). Consequently, we get

$$\sum_{n=0}^{N}\left[D_{1,n}\left(h_c-\alpha k_r\right)+D_{2,n}\left(-h_c+2\alpha k_r\right)\right]\left\langle\phi_n^{\tilde{z}},\phi_i^{\tilde{z}}\right\rangle_{\tilde{z}} = \left\langle u_c,\phi_i^{\tilde{z}}\right\rangle_{\tilde{z}} \tag{27a}$$

$$\sum_{m=0}^{M}\left[D_{3,m}\left(h_t-\beta k_z\right)+D_{4,m}\left(h_t-2\beta k_z\right)\right]\left\langle\phi_m^{\tilde{r}},\phi_j^{\tilde{r}}\right\rangle_{\tilde{r}} = \left\langle u_t,\phi_j^{\tilde{r}}\right\rangle_{\tilde{r}} \tag{27b}$$

$$\sum_{m=0}^{M}\left[D_{3,m}\left(h_b-\beta k_z\right)+D_{4,m}\left(-h_b+2\beta k_z\right)\right]\left\langle\phi_m^{\tilde{r}},\phi_j^{\tilde{r}}\right\rangle_{\tilde{r}} = \left\langle u_b,\phi_j^{\tilde{r}}\right\rangle_{\tilde{r}} \tag{27c}$$

where the notation $\langle f,\phi_j^{\tilde{r}}\rangle_{\tilde{r}}=\int_{-1}^{1} rf(\tilde{r})\phi_j^{\tilde{r}}(\tilde{r})d\tilde{r}$ represents the 1-D inner product in the $\tilde{r}$-direction and r is included in the inner product to account for cylindrical coordinates. $\phi_j^{\tilde{r}}$ with $j\in\{0,\ldots,M\}$ are the test functions.

For all values of i and j in (26) and (27), there are $2N+2M$ unknown coefficients in $2N+2M$ equations. By solving these equations, we can uniquely determine $D_{1,n}$, $D_{2,n}$, $D_{3,m}$, and $D_{4,m}$ for all n and m. To simplify the notations, along the cell's surface, core, top, and bottom sides, we define

$$\begin{aligned} s_1&=\left(h_s-\alpha k_r\right), \quad & s_2&=\left(h_s-2\alpha k_r\right)\\ t_1&=\left(h_t-\beta k_z\right), \quad & t_2&=\left(h_t-2\beta k_z\right)\\ c_1&=\left(h_c-\alpha k_r\right), \quad & c_2&=\left(-h_c+2\alpha k_r\right)\\ b_1&=\left(h_b-\beta k_z\right), \quad & b_2&=\left(-h_b+2\beta k_z\right). \end{aligned}$$

Then, (26) and (27) can be rewritten as

$$\Phi_v\left(D_1s_1+D_2s_2\right)=u_sS_v \tag{28a}$$

$$\Phi_v\left(D_1c_1+D_2c_2\right)=u_cS_v \tag{28b}$$

$$\Phi_h\left(D_3t_1+D_4t_2\right)=u_tS_h \tag{28c}$$

$$\Phi_h\left(D_3b_1+D_4b_2\right)=u_bS_h \tag{28d}$$

where the matrices for the vertical sides $\Phi_v(\tilde{z})\in\mathcal{R}^{N\times N}$ and the horizontal sides $\Phi_h(\tilde{r})\in\mathcal{R}^{N\times N}$ are given by $\Phi_v=\langle\phi_n^{\tilde{z}},\phi_i^{\tilde{z}}\rangle_{\tilde{z}}$ and $\Phi_h=\langle\phi_m^{\tilde{r}},\phi_j^{\tilde{r}}\rangle_{\tilde{r}}$, respectively. The source terms for the vertical sides $S_v(\tilde{z})\in\mathcal{R}^N$ and the horizontal sides $S_h(\tilde{r})\in\mathcal{R}^M$ are given by $S_v=\langle 1,\phi_i^{\tilde{z}}\rangle_{\tilde{z}}$ and $S_h=\langle 1,\phi_j^{\tilde{r}}\rangle_{\tilde{r}}$, respectively. D_1, D_2, D_3, and D_4 are vectors of the unknown coefficients, explicitly defined as

$$\begin{aligned} D_1&=\begin{bmatrix}D_{1,1} & D_{1,2} & \cdots & D_{1,N}\end{bmatrix}^T\\ D_2&=\begin{bmatrix}D_{2,1} & D_{2,2} & \cdots & D_{2,N}\end{bmatrix}^T\\ D_3&=\begin{bmatrix}D_{3,1} & D_{3,2} & \cdots & D_{3,M}\end{bmatrix}^T\\ D_4&=\begin{bmatrix}D_{4,1} & D_{4,2} & \cdots & D_{4,M}\end{bmatrix}^T. \end{aligned}$$

By solving (28), the coefficient vectors can be determined

$$D_1=\frac{1}{s_1c_2-s_2c_1}\left(c_2u_s-s_2u_c\right)\Phi_v^{-1}S_v \tag{29a}$$

$$D_2=\frac{1}{s_1c_2-s_2c_1}\left(-c_2u_s+s_1u_c\right)\Phi_v^{-1}S_v \tag{29b}$$

$$D_3=\frac{1}{t_1b_2-t_2b_1}\left(b_2u_t-t_2u_b\right)\Phi_h^{-1}S_h \tag{29c}$$

$$D_4=\frac{1}{t_1b_2-t_2b_1}\left(-b_2u_t+t_1u_b\right)\Phi_h^{-1}S_h. \tag{29d}$$

As a result, the particular solution $\hat{T}_p$ in (23) has been derived.

3) Model Decomposition for Independent and Targeted Cooling Control:

Remark 3: Previous efforts in the battery community to derive (9) (see [17], [18]) utilized (23) as their particular solution. However, (23) in its present form does not allow independent and targeted cooling control of battery tabs and surfaces, preventing its use for optimally combining tab and SC for enhanced battery thermal performance.

Different from existing works in the literature, as noted in Remark 3, we propose a new method to derive the particular solution T_p in battery thermal modeling. This method and its resulting model formulation offer the flexibility of independent controls for each side of the cell, including the tabs and surfaces. It is achieved by pertinent model decomposition, in which the key idea is to decompose (23) into four components, each representing a side of the cylindrical battery cell.

According to (29), the coefficient vectors, D_1 and D_2, are functions of u_s and u_c, while D_3 and D_4 are functions of u_t and u_b. With this in mind, we can rearrange (29) so that each coefficient vector is expressed in two terms as

$$\begin{aligned} D_1&=d_1^su_s+d_1^cu_c, \quad & D_2&=d_2^su_s+d_2^cu_c\\ D_3&=d_1^tu_t+d_1^bu_b, \quad & D_4&=d_2^tu_t+d_2^bu_b \end{aligned} \tag{30}$$

where

$$\begin{aligned} d_1^s&=\frac{c_2}{s_1c_2-s_2c_1}\Phi_v^{-1}S_v, \quad & d_2^s&=\frac{-c_2}{s_1c_2-s_2c_1}\Phi_v^{-1}S_v\\ d_1^c&=\frac{-s_2}{s_1c_2-s_2c_1}\Phi_v^{-1}S_v, \quad & d_2^c&=\frac{s_1}{s_1c_2-s_2c_1}\Phi_v^{-1}S_v\\ d_1^t&=\frac{b_2}{t_1b_2-t_2b_1}\Phi_h^{-1}S_h, \quad & d_2^t&=\frac{-b_2}{t_1b_2-t_2b_1}\Phi_h^{-1}S_h\\ d_1^b&=\frac{-t_2}{t_1b_2-t_2b_1}\Phi_h^{-1}S_h, \quad & d_2^b&=\frac{t_1}{t_1b_2-t_2b_1}\Phi_h^{-1}S_h. \end{aligned} \tag{31}$$

Substituting (30) and (31) into (23), we have the new expansion for the particular solution as

$$\begin{aligned} \hat{T}_p\left(\tilde{r},\tilde{z},t\right)=&\sum_{n=0}^{N}\Big[\left(d_1^s\left(\tilde{z}\right)u_s\left(t\right)+d_1^c\left(\tilde{z}\right)u_c\left(t\right)\right)\tilde{r}\\ &+\left(d_2^s\left(\tilde{z}\right)u_s\left(t\right)+d_2^c\left(\tilde{z}\right)u_c\left(t\right)\right)\tilde{r}^2\Big]\phi_n^{\tilde{z}}\left(\tilde{z}\right)\\ &+\sum_{m=0}^{M}\Big[\left(d_1^t\left(\tilde{r}\right)u_t\left(t\right)+d_1^b\left(\tilde{r}\right)u_b\left(t\right)\right)\tilde{z}\\ &+\left(d_2^t\left(\tilde{r}\right)u_t\left(t\right)+d_2^b\left(\tilde{r}\right)u_b\left(t\right)\right)\tilde{z}^2\Big]\phi_m^{\tilde{r}}\left(\tilde{r}\right). \end{aligned} \tag{32}$$

The above result can be reorganized into four components as

$$\begin{aligned} \hat{T}_p\left(\tilde{r},\tilde{z},t\right)=&\hat{T}_p^s\left(\tilde{r},\tilde{z}\right)u_s\left(t\right)+\hat{T}_p^c\left(\tilde{r},\tilde{z}\right)u_c\left(t\right)\\ &+\hat{T}_p^t\left(\tilde{r},\tilde{z}\right)u_t\left(t\right)+\hat{T}_p^b\left(\tilde{r},\tilde{z}\right)u_b\left(t\right) \end{aligned} \tag{33}$$

where $\hat{T}_p^s$, $\hat{T}_p^c$, $\hat{T}_p^t$, and $\hat{T}_p^b$ represent the particular solution expansions projected onto the surface, core, top, and bottom, respectively. Specifically, these components are given by

$$\hat{T}_p^s=\sum_{n=0}^{N}\left(d_1^s\tilde{r}+d_2^s\tilde{r}^2\right)\phi_n^{\tilde{z}}, \quad \hat{T}_p^c=\sum_{n=0}^{N}\left(d_1^c\tilde{r}+d_2^c\tilde{r}^2\right)\phi_n^{\tilde{z}} \tag{34a}$$

$$\hat{T}_p^t = \sum_{m=0}^{M} \left(d_1^t \tilde{z} + d_2^t \tilde{z}^2\right) \phi_m^{\tilde{r}}, \quad \hat{T}_p^b = \sum_{m=0}^{M} \left(d_1^b \tilde{z} + d_2^b \tilde{z}^2\right) \phi_m^{\tilde{r}}. \tag{34b}$$

We recall from (8) that $u_c = 0$ for the cylindrical cell, thus $\hat{T}_p^c$ does not contribute to the particular solution. Due to this, we neglect $\hat{T}_p^c$ in the sequel.

Remark 4: The result obtained in (33) and (34) implies that for the particular problem in (13), which leads to the particular solution T_p featuring linearity in two spatial dimensions, the solution trajectory in response to the cooling power applied at each individual boundary satisfies the superposition principle. Additionally, the particular solution $T_p(\tilde{r}, \tilde{z}, t)$ at each position $(\tilde{r}, \tilde{z})$ can be expressed as a linear combination of the cooling powers applied at different boundaries.

E. State-Space Model Representation

Substituting the particular solution in (33) and (34) into (12) and using the linearity of the partial differential operator, the term q^*, which is required for deriving the homogeneous solution T_h, can be obtained accordingly

$$\begin{aligned} q^* = q &+ \left[\alpha^2 k_r \frac{\partial^2 \hat{T}_p^s}{\partial \tilde{r}^2} + \gamma \frac{\partial \hat{T}_p^s}{\partial \tilde{r}} + \beta^2 k_z \frac{\partial^2 \hat{T}_p^s}{\partial \tilde{z}^2}\right] u_s \\ &+ \left[\alpha^2 k_r \frac{\partial^2 \hat{T}_p^t}{\partial \tilde{r}^2} + \gamma \frac{\partial \hat{T}_p^t}{\partial \tilde{r}} + \beta^2 k_z \frac{\partial^2 \hat{T}_p^t}{\partial \tilde{z}^2}\right] u_t \\ &+ \left[\alpha^2 k_r \frac{\partial^2 \hat{T}_p^b}{\partial \tilde{r}^2} + \gamma \frac{\partial \hat{T}_p^b}{\partial \tilde{r}} + \beta^2 k_z \frac{\partial^2 \hat{T}_p^b}{\partial \tilde{z}^2}\right] u_b. \end{aligned} \tag{35}$$

Based on the results in Sections III-C and III-D, a control-oriented 2-D thermal model of cylindrical battery cells is achieved. We define X as the state variable, u the input, $\mathcal{Y}$ the output, and w the disturbance. According to Section III-C, X is given by

$$X = [c_{11}, \ldots, c_{1N}, c_{21}, \ldots, c_{2N}, \ldots, c_{M1}, \ldots, c_{MN}]^T. \tag{36}$$

The input u is composed of the cooling power applied at the different places, leading to $u = [u_s, u_t, u_b]^T$. The disturbance w represents the heat generation rate, namely $w = q$. The outputs of interest, $\mathcal{Y}$, include the temperatures at the mid-points of the surface, core, top, and bottom sides, namely

$$\mathcal{Y}(t) = \left[\hat{T}(1,0,t)\ \hat{T}(-1,0,t)\ \hat{T}(0,1,t)\ \hat{T}(0,-1,t)\right]^T \tag{37}$$

where $\hat{T}$ is the approximate solution of T in (9). With these definitions, this dynamic thermal model can be presented in the state-space form

$$\mathcal{G}\dot{X}(t) = \mathcal{A}X(t) + \mathcal{B}u(t) + \mathcal{F}w(t) \tag{38a}$$

$$\mathcal{Y}(t) = \mathcal{C}X(t) + \mathcal{D}u(t) \tag{38b}$$

where with the additional term

$$\mathcal{D} = \begin{bmatrix} \hat{T}_p^s(1,0) & \hat{T}_p^t(1,0) & \hat{T}_p^b(1,0) \\ \hat{T}_p^s(-1,0) & \hat{T}_p^t(-1,0) & \hat{T}_p^b(-1,0) \\ \hat{T}_p^s(0,1) & \hat{T}_p^t(0,1) & \hat{T}_p^b(0,1) \\ \hat{T}_p^s(0.-1) & \hat{T}_p^t(0.-1) & \hat{T}_p^b(0.-1) \end{bmatrix} \tag{39}$$

the matrices $\mathcal{G}$, $\mathcal{A}$, $\mathcal{B}$, $\mathcal{C}$, and the vector $\mathcal{F}$ are derived from (9), (12), Section III-C, and (33) and (34) to yield

$$\mathcal{G} = \rho c_p \left\langle r \phi_m^{\tilde{r}} \phi_n^{\tilde{z}}, \eta \right\rangle \tag{40a}$$

$$\mathcal{A} = \left\langle r \left[\alpha^2 k_r \frac{\partial^2 \phi_m^{\tilde{r}} \phi_n^{\tilde{z}}}{\partial \tilde{r}^2} + \gamma \frac{\partial \phi_m^{\tilde{r}} \phi_n^{\tilde{z}}}{\partial \tilde{r}} + \beta^2 k_z \frac{\partial^2 \phi_m^{\tilde{r}} \phi_n^{\tilde{z}}}{\partial \tilde{z}^2}\right], \eta \right\rangle \tag{40b}$$

$$\mathcal{B}(:,1) = \left\langle r \left[\alpha^2 k_r \frac{\partial^2 \hat{T}_p^s}{\partial \tilde{r}^2} + \gamma \frac{\partial \hat{T}_p^s}{\partial \tilde{r}} + \beta^2 k_z \frac{\partial^2 \hat{T}_p^s}{\partial \tilde{z}^2}\right], \eta \right\rangle \tag{40c}$$

$$\mathcal{B}(:,2) = \left\langle r \left[\alpha^2 k_r \frac{\partial^2 \hat{T}_p^t}{\partial \tilde{r}^2} + \gamma \frac{\partial \hat{T}_p^t}{\partial \tilde{r}} + \beta^2 k_z \frac{\partial^2 \hat{T}_p^t}{\partial \tilde{z}^2}\right], \eta \right\rangle \tag{40d}$$

$$\mathcal{B}(:,3) = \left\langle r \left[\alpha^2 k_r \frac{\partial^2 \hat{T}_p^b}{\partial \tilde{r}^2} + \gamma \frac{\partial \hat{T}_p^b}{\partial \tilde{r}} + \beta^2 k_z \frac{\partial^2 \hat{T}_p^b}{\partial \tilde{z}^2}\right], \eta \right\rangle \tag{40e}$$

$$\mathcal{C}(1,:) = \phi_m^{\tilde{r}}(1)\phi_n^{\tilde{z}}(0), \quad \mathcal{C}(2,:) = \phi_m^{\tilde{r}}(-1)\phi_n^{\tilde{z}}(0) \tag{40f}$$

$$\mathcal{C}(3,:) = \phi_m^{\tilde{r}}(0)\phi_n^{\tilde{z}}(1), \quad \mathcal{C}(4,:) = \phi_m^{\tilde{r}}(0)\phi_n^{\tilde{z}}(-1) \tag{40g}$$

$$\mathcal{F} = \langle r \cdot 1, \eta \rangle. \tag{40h}$$

Up to this point, the initial PDE-based model for cylindrical battery cells governed by (1) and (2) has been reformulated and approximated by the above ODE-based model. The order of this model, which is also called the number of states, is $O = MN$.

F. Application of the Modeling Techniques to Pouch Cells

The modeling techniques introduced in Sections III-A–III-E can also be applied to pouch battery cells. For brevity, only the key mathematical results are presented.

As a result of nondimensionalization, the initial thermal model for pouch cells in (3) and (4) can be presented in the form

$$\rho c_p \frac{\partial T}{\partial t} - \lambda^2 k_x \frac{\partial^2 T}{\partial \tilde{x}^2} - \zeta^2 k_y \frac{\partial^2 T}{\partial \tilde{y}^2} = q \tag{41}$$

with scaling factors $\lambda = 2/D$ and $\zeta = 2/H$. The new spatial coordinates are $\tilde{x} = 2x/D - 1$ and $\tilde{y} = 2y/H - 1$. The above dynamic equation is subject to the boundary conditions

$$h_{fs} T - \lambda k_x \frac{\partial T}{\partial \tilde{x}} = u_{fs} \quad \text{at } \tilde{x} = 1 \tag{42a}$$

$$-h_{bs} T - \lambda k_x \frac{\partial T}{\partial \tilde{x}} = u_{bs} \quad \text{at } \tilde{x} = -1 \tag{42b}$$

$$h_t T - \zeta k_y \frac{\partial T}{\partial \tilde{y}} = u_t \quad \text{at } \tilde{y} = 1 \tag{42c}$$

$$-h_b T - \zeta k_y \frac{\partial T}{\partial \tilde{y}} = u_b \quad \text{at } \tilde{y} = -1 \tag{42d}$$

where u_{fs}, u_{bs}, u_t, and u_b represent the cooling power applied per unit area at the front, back, top, and bottom sides of the pouch cell, respectively, which are mathematically defined as

$$u_{fs}(t) = h_{fs}(t) T_{fs,\infty}(t), \quad u_{bs}(t) = -h_{bs}(t) T_{bs,\infty}(t) \tag{43a}$$

$$u_t(t) = h_t(t) T_{t,\infty}(t), \quad u_b(t) = -h_b(t) T_{b,\infty}(t). \tag{43b}$$

The outputs of interest $\mathcal{Y}$, for pouch battery cells, are located at the middle of each side, with the mathematical definition being the same as (37).

Following similar steps from (9)–(35), the battery model in (41)–(42) can also be approximated by an ODE-based model in the state-space form of (38) with the state variable defined in (36) and the input $u = [u_{fs},\ u_{bs},\ u_t,\ u_b]^T$. The resulting matrices and vectors for this state-space model are given by

$$\mathcal{G} = \rho c_p \left\langle \phi_m^{\tilde{x}} \phi_n^{\tilde{y}}, \eta \right\rangle \tag{44a}$$

$$\mathcal{A} = \left\langle \lambda^2 k_x \frac{\partial^2 \phi_m^{\tilde{x}} \phi_n^{\tilde{y}}}{\partial \tilde{x}^2} + \zeta^2 k_y \frac{\partial^2 \phi_m^{\tilde{x}} \phi_n^{\tilde{y}}}{\partial \tilde{y}^2}, \eta \right\rangle \tag{44b}$$

$$\mathcal{B}(:,1) = \left\langle \lambda^2 k_x \frac{\partial^2 \hat{T}_p^{fs}}{\partial \tilde{x}^2} + \zeta^2 k_y \frac{\partial^2 \hat{T}_p^{fs}}{\partial \tilde{y}^2}, \eta \right\rangle \tag{44c}$$

$$\mathcal{B}(:,2) = \left\langle \lambda^2 k_x \frac{\partial^2 \hat{T}_p^{bs}}{\partial \tilde{x}^2} + \zeta^2 k_y \frac{\partial^2 \hat{T}_p^{bs}}{\partial \tilde{y}^2}, \eta \right\rangle \tag{44d}$$

$$\mathcal{B}(:,3) = \left\langle \lambda^2 k_x \frac{\partial^2 \hat{T}_p^{t}}{\partial \tilde{x}^2} + \zeta^2 k_y \frac{\partial^2 \hat{T}_p^{t}}{\partial \tilde{y}^2}, \eta \right\rangle \tag{44e}$$

$$\mathcal{B}(:,4) = \left\langle \lambda^2 k_x \frac{\partial^2 \hat{T}_p^{b}}{\partial \tilde{x}^2} + \zeta^2 k_y \frac{\partial^2 \hat{T}_p^{b}}{\partial \tilde{y}^2}, \eta \right\rangle \tag{44f}$$

$$\mathcal{C}(1,:) = \phi_m^{\tilde{x}}(1)\,\phi_n^{\tilde{y}}(0),\quad \mathcal{C}(2,:) = \phi_m^{\tilde{x}}(-1)\,\phi_n^{\tilde{y}}(0) \tag{44g}$$

$$\mathcal{C}(3,:) = \phi_m^{\tilde{x}}(0)\,\phi_n^{\tilde{y}}(1),\quad \mathcal{C}(4,:) = \phi_m^{\tilde{x}}(0)\,\phi_n^{\tilde{y}}(-1) \tag{44h}$$

$$\mathcal{F} = \langle 1, \eta \rangle \tag{44i}$$

where $\hat{T}_p^{fs}$ and $\hat{T}_p^{bs}$ represent the particular solutions of the front- and back-side expansions, respectively.

At higher C-rates, localized heat generation at the battery tabs can significantly influence the internal temperature distribution of the cell [26]. Future work will explore modeling approaches that treat the tabs and cell body as thermally coupled regions. This will enable a more spatially resolved thermal analysis and better capture the impact of tab heating on overall cell performance.

Due to the internal structure of prismatic cells, significant thermal gradients can develop in all space dimensions (x, y, and z), requiring a 3D thermal model for better accuracy. However, the underlying solution processes for the prismatic cell are equivalent to those of the cylindrical and pouch cells provided in Sections III-C and III-D.

IV. Model Validation and Evaluation

In this section, we evaluate the developed spatially distributed thermal models for cylindrical battery cells in (38)–(40) and for pouch cells in (38) and (44). In addition to the computational efficiency, the evaluation criteria include model accuracy for the maximum temperature $T_{\max}$, mean temperature T_{mean}, maximum thermal gradient along the radius direction $\delta T_{\max}^r$, maximum thermal gradient along the axial direction $\delta T_{\max}^z$, and mean thermal gradient δT_{mean}^r. Then, we incorporate these models in a feedback controller for battery cooling and investigate the effectiveness of various tab and SC scenarios. Additionally, using cylindrical cells as an example, we study the influence of varying dimensions on battery thermal performance.

A. Benchmarks

To comprehensively and systematically assess the proposed modeling approach, we introduce two types of benchmarks. The first type is the original PDE models, that is, (1)–(4), solved by the FEM. Results from these models will serve as ground truth in comparative studies. The second type of benchmark is TEC models that are widely studied in the literature [12], [13], [27], [28], and have been utilized in commercial BMSs. This kind of model features lumped parameters and two states in the form

$$C_c \dot{T}_c(t) = q(t) + \frac{T_s(t) - T_c(t)}{R_c} \tag{45a}$$

$$C_s \dot{T}_s(t) = \frac{T_\infty - T_s(t)}{R_u} + \frac{T_s(t) - T_c(t)}{R_c} \tag{45b}$$

where T_c and T_s represent the core and surface temperatures, respectively. R_c is the heat conduction resistance, which quantifies the heat exchange between the core and surface. R_u is the convection resistance, which measures the convection cooling along the battery surface and is dependent on the pack geometry, coolant type, and flow rate. C_c and C_s indicate the heat capacity of the core and surface (casing), respectively.

To utilize the TEC model in (45), we first need to identify the unknown parameters, that is, C_c, C_s, R_c, and R_u, for given battery cells and cooling scenarios. We follow the parameterization scheme proposed in [13], which was designed using the least-squares algorithm and the measurable current I (or q), T_s, and T_∞. According to [13], only three of the four parameters can be identified from these measurements, and one parameter must be assumed. In fact, the heat capacity of the aluminum casing C_s can be calculated from its specific heat capacity and dimensions.

B. Specification and Simulation Setup

To evaluate the modeling for cylindrical cells, we choose a large-format lithium-iron-phosphate (LFP) 45Ah cell and take the corresponding model parameters from [29]. Specifically, for dimension-related parameters, we have $L = 198$ mm, $R_{\text{out}} = 32$ mm, $R_{\text{in}} = 4$ mm [29], and for thermo-physical parameters, we use $\rho = 2118\ \text{kgm}^{-3}$, $c_p = 795\ \text{Jkg}^{-1}\text{K}^{-1} k_r = 0.67\ \text{Wm}^{-1}\text{K}^{-1}$, and $k_z = 66.6\ \text{Wm}^{-1}\text{K}^{-1}$ [13], [30]. For the TEC model of this cylindrical cell, C_s is found to be $48.35\ \text{JK}^{-1}$. Regarding R_c and R_u, it is important to note that different sets of parameters will be obtained, depending on the employed cooling scenario. For brevity, only the identified parameters for SC are presented here. After validation, we obtained the parameter values as $C_c = 1079.6\ \text{JK}^{-1}$, $R_c = 0.65\ \text{KW}^{-1}$, and $R_u = 0.08\ \text{KW}^{-1}$.

In the simulation-based study of the proposed battery models and their benchmarks, the initial temperatures, that is, $T(r,z,0)$, $T(x,y,0)$, $T_c(0)$, and $T_s(0)$, and the fluid free-stream (ambient) temperature T_∞ are all chosen to be 15 °C. To facilitate the study without losing generality, the volumetric heat generation rate q is given by the heat generation model proposed by Bernardi et al. [31]

$$q(t) = I(t)\left[V(t) - V_{\text{ocv}}(t)\right]/V_b \tag{46}$$

where I, V, V_{ocv}, and V_b are the battery current, terminal voltage, open-circuit voltage, and volume, respectively. Here, the trajectories of I and V depend on the battery usage. We select the worldwide harmonized light vehicle test procedure (WLTP) [32], which represents a wide range of vehicle driving

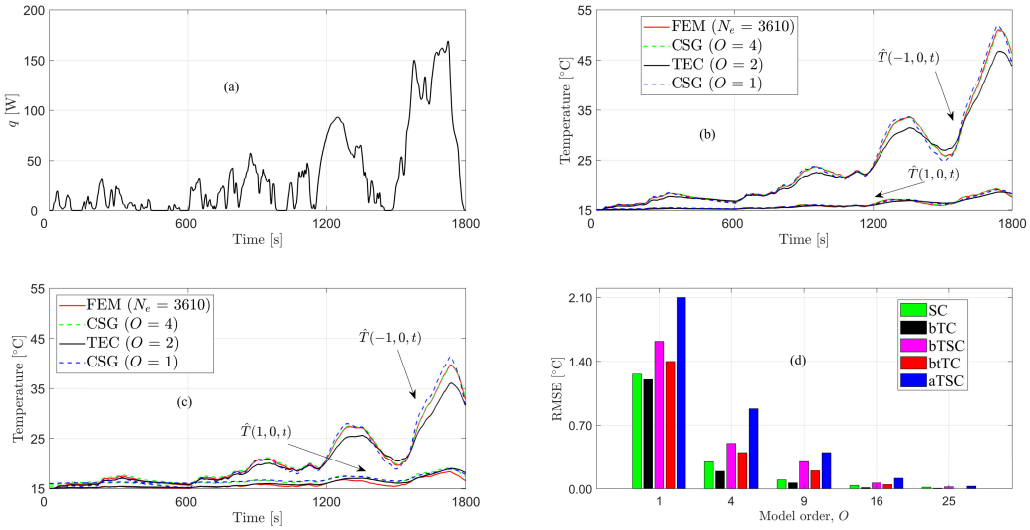

Fig. 2. Validation of the developed CSG thermal model for cylindrical battery cells. (a) Heat generation profile of the mWLTP. (b) Comparison of the CSG model of orders $O = 1$ and 4, against the FEM model with the element number $N_e = 3610$ and TEC model, under SC. Comparisons are done for the surface and core midpoint temperatures, that is, $\hat{T}(1,0,t)$ and $\hat{T}(-1,0,t)$. (c) Comparison of the CSG thermal model against FEM and TEC models under the scenario of all-tabs and SC (aTSC). (d) Maximum error of the CSG model with different orders under all cooling cases.

conditions on urban, suburban, and highway roads, and scale it so that the maximum current becomes 1 C-rate for heat generation. The modified WLTP (mWLTP) heat generation profile is shown in Fig. 2(a). V_{ocv} depends on the state of charge (SoC), and the relationship between V_{ocv} and SoC has been determined using a lookup table for a typical LFP cell in [33].

Depending on where the cooling action is imposed, five different cooling scenarios are investigated, including SC, bottom tab cooling (bTC), bottom tab and SC (bTSC), bottom and top tabs cooling (btTC), and all-tabs and SC (aTSC). aTSC has all sides of the battery cell exposed to cooling and is representative of immersion cooling [34] where the cell is immersed in a dielectric fluid. Forced convection liquid cooling (for instance, using a cooling plate) via water or glycol is considered to apply to areas where tab or SC occurs. This typically has a large convection coefficient h, which is set to be 400 $\text{Wm}^{-2}\text{K}^{-1}$, according to [4]. For areas not exposed to active liquid cooling, mild forced air convection occurs, resulting in a small convection coefficient specified as $h = 30$ $\text{Wm}^{-2}\text{K}^{-1}$.

All the simulations are conducted on a MacBook Pro with a 2.6 GHz 6-Core Intel Core i7 processor and 16GB RAM. The first type of benchmark model is solved by the FEM with an extremely fine mesh of 3610 triangular elements and is implemented in COMSOL Multiphysics v6.0 [35]. Our developed CSG models and their TEC alternatives are implemented in MATLAB R2023b. For simplicity in simulating the CSG models, the number of basis functions in the radial and axial directions, as introduced in (15), is chosen to be equal, that is, $M = N$, and the model order $O = N^2$.

C. Results of Validation Against the FEM Model

The examination of the developed modeling method and its underlying assumptions for control-oriented applications is conducted for the battery cell and cooling scenarios specified in Section IV-B. Different CSG model orders, including $O = 1$, 4, 9, 16, and 25, were evaluated. The results for cylindrical cell modeling compared with the ground truth represented by the FEM model are presented in Fig. 2.

TABLE I
EFFECT OF CURRENT RATES ON MODEL ACCURACY

Current profile	O=1	O=4	O=9	O=16	O=25
mWLTP	1.26	0.46	0.13	0.09	0.03
mWLTP×2	3.83	2.36	1.11	0.98	0.73
mWLTP×3	4.89	3.62	1.85	1.36	1.01

According to Fig. 2(d), the developed CSG model with an order of 25 can almost perfectly capture the battery cell's distributed thermal dynamics under any of the considered cooling scenarios. The resulting modeling error is bounded by 0.03 °C. Reducing the model order from 25 to 9, the maximum temperature deviation between the model's output and its ground truth is 0.4 °C within the entire test process. Similar observations are obtained for the studied pouch cell, in which the prediction error for the model with an order of 9 is less than 0.6 °C. Remarkably, this high level of model fidelity is achieved in the presence of aggressive driving and cooling. The prediction error gradually increases when the model order is further lowered. This is consistent with *Remark 2* and the applied finite-sum approximations in (14) and (23). Indeed, the model with an order of 1 or 4 can still follow the trajectories of the true surface and core temperatures under different cooling scenarios, as seen in Fig. 2(b) and (c). Specifically, for SC, which involves one-sided cooling, $O = 1$ results in a maximum error of 1.26 °C. For a TSC, which involves resolution in multiple directions (multiside cooling), the same order produces a maximum error of 2.10 °C.

The impact of current rates on model accuracy is also evaluated. To do so, the mWLTP profile is scaled by factors of two and three, resulting in maximum C-rates of 2C and 3C, respectively. Under these highly aggressive operating conditions and the SC scenario, the errors of the CSG model with different orders are summarized in Table I. The results

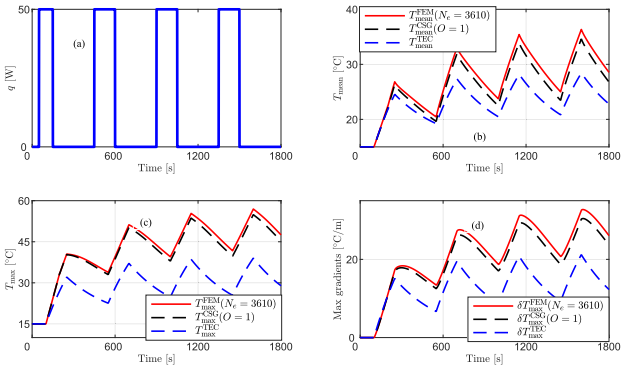

Fig. 3. Comparison between the CSG and TEC models under SC. (a) Pulse heat generation profile. (b) Evaluation of the mean temperature responses of the two models, that is, $T^{\text{CSG}}_{\text{mean}}$ and $T^{\text{TEC}}_{\text{mean}}$, against their ground truth. (c) Comparison of their max temperature responses, which are $T^{\text{CSG}}_{\text{max}}$ and $T^{\text{TEC}}_{\text{max}}$. (d) Maximum thermal gradients of the CSG and TEC models, that is, $\delta T^{\text{CSG}}_{\text{max}}$ and $\delta T^{\text{TEC}}_{\text{max}}$.

demonstrate a clear necessity to increase the model order for accurately capturing battery cell thermal dynamics at elevated current rates due to pronounced thermal gradients and intensified spatial interactions. Considering a maximum permissible error of 1.5 °C, model orders $O = 1$, 9, and 16 are sufficient to faithfully model the thermal behavior in the mWLTP, mWLTP×2, and mWLTP×3 scenarios, respectively. It is worth mentioning that with this relatively small magnitude of local errors obtained under all considered cooling scenarios and extreme battery usage conditions, the CSG model proves suitable for a wide range of battery management applications.

The above results consequently verify the effectiveness of the modeling approach proposed in Section III. Specifically, this confirms that the developed adaptable approach for the particular solution T_p can efficiently handle any abrupt changes in the operating conditions and spatial gradients distributed across the battery cell; the CSG method can well reproduce the state dynamics governed by the PDE and its homogeneous solution. Furthermore, it numerically proves the conclusions drawn in Remark 4. Namely, for the particular solution problem in (13), the response to the cooling power applied at individual boundaries satisfies the superposition principle and can be expressed as a linear combination of the cooling power applied at these boundaries.

In addition to the above validation against the high-fidelity FEM model implemented in COMSOL, our future work will explore direct experiments to evaluate our model under various cooling configurations.

D. Results of Comparison Against the TEC Model

To investigate the efficacy and applicability of the CSG model validated in Section IV-C, we compare it with the second type of benchmark defined in Section IV-A, that is, the TEC model. In the TEC model, the average temperature is derived as $T^{\text{TEC}}_{\text{mean}} = (T_s + T_c)/2$, and the radial gradient is defined by $\delta T^r_{max} = (T_c - T_s)/(R_{\text{out}} - R_{\text{in}})$. To possibly fully reveal their predictive capability, particularly under highly dynamic operating conditions, we introduce a pulsed power load profile to generate the heat $q(t)$, as shown in Fig. 3(a). This heat trajectory is characterized by high heat generation rates but a relatively short duration. For completeness, the TEC model was also included in the WLTP validation scenario shown in Fig. 2(b) and (c). The comparative results between the FEM, CSG, and TEC models under the pulsed power profile with SC are presented in Fig. 3.

TABLE II
AVERAGE COMPUTATIONAL TIMES OF THE CSG MODEL OF DIFFERENT ORDERS COMPARED WITH THE TEC MODEL

Model type	FEM	TEC	O=1	O=4	O=9	O=16	O=25
Time [ms]	8000	307	219	431	517	652	746

It is found that the CSG model of $O = 1$ is capable of closely following the true trajectories of the mean temperature, max temperature, and max gradient in the entire test cycle. By contrast, in general, the TEC model with an order of 2 significantly underestimates all three considered indicators, resulting in temperature errors of several degrees. To observe more closely, the model's error for T_{max} is much larger than that for T_{mean}, and it increases when there are abrupt changes in the heat generation. This observation is consistent with the comparison under the WLTP profile in Fig. 2(b) and (c), where the TEC model similarly underestimates the core and surface temperatures. This means that compared to our developed model, the TEC model is unreliable for predicting the local thermal behavior and may be limited to applications with only low heat generation in the battery cell. Particularly, this model cannot be used for battery safety management, where the maximum temperature must be accurately estimated and constrained, and for thermal uniformity control, where the information on the maximum gradients is critical.

Computational efficiency is of great importance for model-based applications, particularly real-time thermal optimization and control of large-scale battery packs. With this in mind, we examine the computational times of the developed model with various orders and compare them with those of the TEC and FEM models. To have a fair comparison, we run each model ten times and compute its average simulation times in milliseconds (ms), with the results listed in Table II. Clearly, the CSG model with an order $O = 1$ is more efficient than its TEC counterpart, leading to a reduction of 28.7% in the required time. The model with higher orders takes longer to simulate, but its time consumption remains within the same order of magnitude as that of the TEC model. As expected, the FEM model takes a longer computational time, about 8s to compute the solution, making it impractical for real-time control applications.

The above results indicate that the CSG model with $O = 1$ offers distinct advantages in both accuracy and computational efficiency. Therefore, it can readily replace the TEC model in existing BMSs to improve battery thermal performance in the real world. In addition, it may be computationally feasible to use a high-order CSG model, for example, the order of 4, within a BMS, allowing a significantly more advanced management of battery safety and lifetime.

V. MODEL-BASED APPLICATIONS

The developed models for cylindrical and pouch battery cells, featuring high fidelity and efficiency, can be effectively applied to various model-based applications. These include

TABLE III
THERMAL PERFORMANCE MERITS UNDER THE FIVE SCENARIOS

Scenarios	T_{mean}	$T_{\max}$	$\delta T^r_{\max}$	$\delta T^z_{\max}$	ΔT
SC	20.80	51.00	32.10	**0.44**	36.00
bTC	22.77	54.01	14.05	8.94	39.01
bTSC	19.38	46.18	27.55	6.70	31.22
btTC	20.29	43.36	**9.32**	3.40	**23.37**
aTSC	**18.30**	**39.68**	21.42	3.17	24.70

rapid analysis of different cooling scenarios, real-time closed-loop temperature control, and thermal assessment of cell dimensions, as demonstrated in this section. Here, based on the model of 9th order, simulations are conducted under the mWLTP profile on the battery cell and cooling scenarios specified in Section IV-B.

A. Model-Based Analysis for Different Cooling Scenarios

For a given battery system and usage profiles, selecting the most appropriate cooling scenario can make a big difference to all its key properties. We analyze thermal performance merits, T_{mean}, $T_{\max}$, $\delta T^r_{\max}$, $\delta T^z_{\max}$, and $\Delta T = T_{\max} - T_{\min}$, under the five cooling scenarios defined in Section IV-B, with the results for cylindrical cells presented in Table III.

In terms of T_{mean}, bTC gives rise to the highest value at 22.77 °C, followed by SC with the second-highest value. This is because the average temperature is primarily influenced by the cooling area, and both bTC and SC have only one side exposed to cooling. With the largest cooling area, aTSC demonstrates a high capability of heat removal, leading to the lowest values of T_{mean} and $T_{\max}$ among all cases. However, aTSC does not achieve the lowest thermal gradient. In contrast, btTC provides the lowest $\delta T^r_{\max}$ at the local level and the lowest ΔT across the entire cell. This can be attributed to symmetric cooling from the cell's top and bottom sides, and all electrodes get access to cooling at the same time under btTC because of the rolled electrode layer structure. On the contrary, in the case of SC, the outer layers get cooled before the internal layers, leading to inhomogeneous cooling and consequently the highest gradient of 32.1 °C/mm.

In all scenarios, it is observed that the cylindrical cell experiences significantly higher thermal gradients along the radial direction compared to the axial direction. This is due to the radial thermal conductivity being two orders of magnitude lower than that of the axial direction, creating a significant bottleneck in heat transfer to the surface. This, combined with the absence of cooling applied to the core, explains why the core temperature is the highest. Increasing the cooling flow rate and using battery materials with higher thermal conductivity can enhance cooling efficiency and help reduce the core temperature.

Moreover, it is evident that no single cooling scenario consistently outperforms the others across all performance metrics. Cooling only one of the cell's tabs, as represented by bTC and bTSC, is unfavorable due to its low removed heat and the significant $\delta T^z_{\max}$. When the cell's surface is involved in cooling, as in SC, bTSC, and aTSC, a considerable $\delta T^r_{\max}$ is observed. Among SC, btTC, and aTSC, each scenario performs the best in one or two specific metrics. For example, btTC offers the most homogeneous cooling effect but results in a slightly higher T_{mean}, whereas aTSC lowers T_{mean} at the cost of increasing $\delta T^r_{\max}$. This indicates that different performance metrics may compete within each cooling scenario.

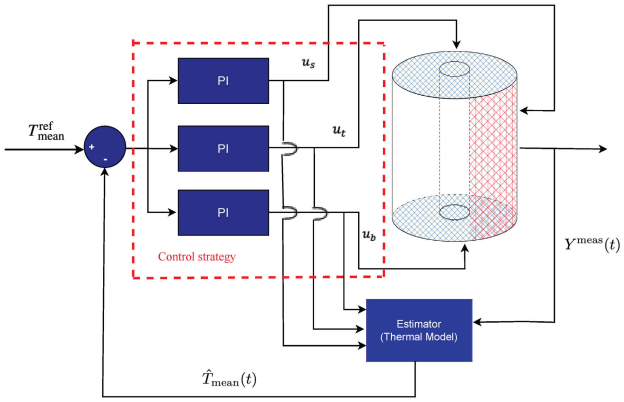

Fig. 4. PI-based control scheme that tracks a given reference for the cylindrical cell's average temperature. $T^{\text{ref}}_{\text{mean}}$ and $\hat{T}_{\text{mean}}$ represent the set-point and estimate of the average temperature, respectively, and Y^{meas} is the cell's measurable outputs. The cooling power applied to the surface, top, and bottom, which are u_s, u_t, and u_b defined in (8), is regulated by their corresponding PI controllers. Their design parameters are set based on the specific cooling scenario.

B. Closed-Loop Temperature Control

The performance tradeoffs revealed in Section V-A necessitate the selection of a scenario to satisfy application-specific requirements. In this regard, an interesting question is: which cooling scenario produces the lowest thermal gradient while maintaining a fixed average temperature?

To answer this question and demonstrate the application of our developed battery thermal models, we implement a simple feedback control strategy based on multiple PI controllers, as framed in Fig. 4. This control scheme is designed to maintain the average cell temperature, T_{mean}, at a predefined set-point, $T^{\text{ref}}_{\text{mean}}$, which is specified as 20 °C. For each cooling scenario, the control in the framework of Fig. 4 is tailored so that individual PI controllers regulate the cooling power directed to specific sides of the cell. For example, in the case of aTSC, all the top, bottom, and surface controllers are active, while for SC, only the surface controller is engaged, with $u_t(t) = u_b(t) = 0$. To simplify the control implementation, we assume a uniform distribution of cooling power across all active areas.

Since T_{mean} is not measurable during real-world battery operation, it is imperative to incorporate a state estimator within the designed control strategy. In this preliminary study, we design an open-loop estimator that mirrors the model (38)–(40) for cylindrical battery cells. However, the state-space model allows any standard state-estimator such as the Kalman filter. Beyond its high accuracy and efficiency, this thermal model enables precise control of cooling applied to any side of the cell or combinations thereof, which is a capability not offered by existing models such as those in [17] and [18]. This flexibility makes our model particularly suitable for battery temperature estimation and control in sophisticated cooling scenarios.

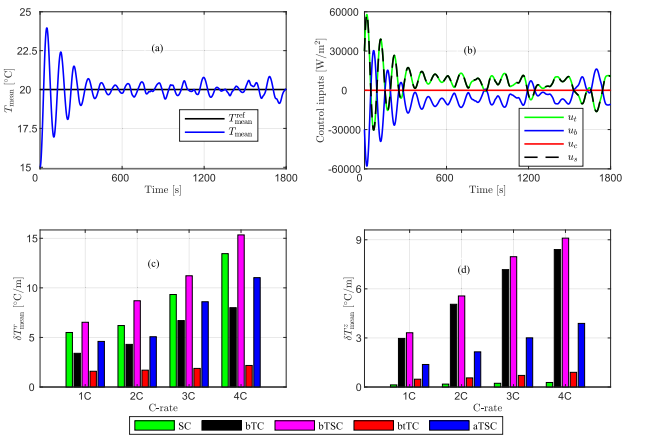

Fig. 5. Results of battery thermal control of the cylindrical cell. (a) and (b) Results obtained in aTSC and the 1 C case of WLTP. (c) and (d) Compare the mean values of the radial and axial thermal gradients, respectively, for different cooling scenarios and WLTP cases.

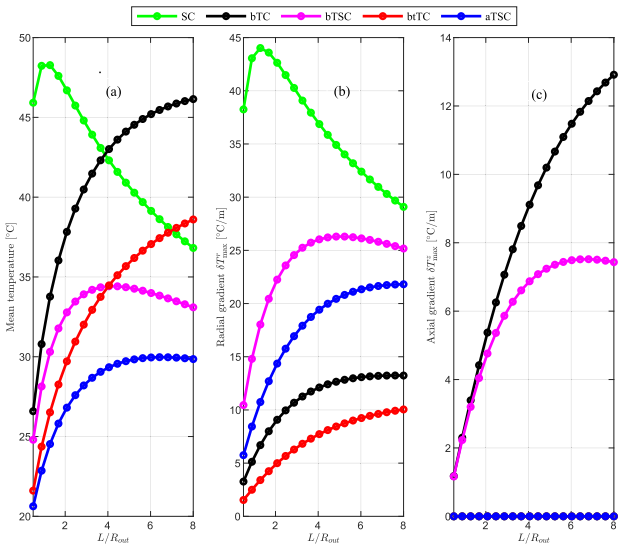

Fig. 6. Evaluation of the thermal performance of cylindrical cells with varying dimensions under five cooling scenarios. (a) Evolution of the mean temperature T_{mean}. (b) Evolution of the maximal thermal gradients in the radial direction $\delta T^r_{\max}$. (c) Evolution of the maximal thermal gradients in the axial direction $\delta T^z_{\max}$.

For case studies, the original WLTP profile is scaled so that the maximum current becomes 1, 2, 3, and 4C, respectively. The control results are given in Fig. 5. To save space, in Fig. 5(a) and (b), only the trajectories obtained in aTSC and the 1 C case are depicted.

Based on the results in Fig. 5(c) and (d), one can readily find the answer to the question raised. When the average cell temperature is maintained at 20 °C, btTC best balances the thermal gradients along the r- and z-directions and produces the most homogeneous thermal distribution across the cylindrical cell. Specifically, in btTC, the average thermal gradient along the r-direction, denoted by δT^r_{mean}, is substantially smaller than those observed in all other cooling scenarios. Regarding the average thermal gradient along the z-direction, btTC is comparable to the best-performing scenario, that is, SC.

In terms of the control's behavior, as demonstrated in Fig. 5(a) and (b), substantial control efforts are initially required to attenuate the large tracking errors. Once T_{mean} approaches the set-point, the magnitude of u_t, u_b, and u_s decreases significantly. Note that the temperature reference of 20 °C is used here purely for demonstration purposes—to showcase the responsiveness and precision of the proposed model under stringent conditions. Beyond the PI controller, future work will explore more sophisticated control strategies to systematically enhance the control performance, in which multiple control objectives and potential constraints will be explicitly addressed. Within the control strategy, the new models developed in Section III can serve as efficient tools for accurately simulating and predicting battery thermal states.

C. Model-Based Evaluation of the Cylindrical Cell Aspect Ratio

A cell's geometry includes critical design parameters that dictate its intrinsic thermal resistance and interface with the thermal management system. We utilized our proposed model to investigate this relationship by performing a parameter sweep on the cell aspect ratio, that is, L/R_{out}. During this study, the total cell volume V_b was held constant so that the heat generation trajectory $q(t)$ under the mWLTP remained identical across all geometries. Fig. 6 shows that the optimal aspect ratio is not universal; instead, it depends strongly on the cooling strategy employed.

The observed behaviors can be grouped into two physical regimes. The first regime includes the four scenarios involving tab cooling, namely, bTC, bTSC, btTC, and aTSC. In these cases, the thermal behavior is conduction-limited. The trends are monotonic: short and bulky cells corresponding to low aspect ratios yield lower mean temperatures and smaller gradients. As the aspect ratio increases, performance degrades because tall, slim cells introduce a long, high-resistance axial conduction path. This impedes heat transfer from the cell's core to the actively cooled tabs, causing heat accumulation. Among these scenarios, aTSC produces the lowest mean temperatures across all aspect ratios due to its larger total cooling area, whereas btTC achieves the lowest radial gradients because of the symmetric cooling applied at both the top and bottom tabs. Axial gradients, although small compared to radial gradients, are nonzero in asymmetrical cooling cases (bTC and bTSC) where $h_t \neq h_b$, and these gradients grow with an increasing aspect ratio. In contrast, for symmetric cases (btTC, SC, and aTSC), where $h_t = h_b$, the axial gradients are identically zero.

The second regime consists of lateral surface-only cooling (SC), which exhibits a different trend. Here, the system is surface-area-limited. For a fixed volume $V_b = \pi(R^2_{\text{out}} - R^2_{\text{in}})L$, the available cooling surface area is $2\pi R_{\text{out}}L$. The corresponding surface-area-to-volume ratio, $2R_{\text{out}}/(R^2_{\text{out}} - R^2_{\text{in}})$, is maximized when radius R_{out} is small, that is, for tall, slim cells. The simulation results confirm this: after a brief rise at very low L/R_{out}, both mean temperature and radial gradients decrease almost linearly with increasing aspect ratio. While performance improves for tall cells due to their larger heat-exchange area, the absolute magnitudes of temperature and radial gradients remain significantly higher than those achieved

with tab-involved cooling. Notably, the mean temperature under SC becomes lower than in bTC and btTC beyond aspect-ratio crossover points of roughly 4 and 5, respectively, but even at these crossovers, the corresponding thermal gradients under SC remain substantially larger. Overall, SC benefits tall, slender geometries, but is generally insufficient as a standalone strategy when uniformity or minimal gradients are required.

These insights also allow us to evaluate commonly used cylindrical cell formats in today's market. The popular 18 650, 21 700, 26 650, and 4680 cells have corresponding L/R_{out} ratios of 7.22, 6.67, 5.00, and 3.48, respectively. Based on our analysis, the 4680 format, thanks to its relatively low aspect ratio, offers improved thermal behavior for all cooling strategies involving tab contact, since its short axial conduction path promotes efficient heat removal. Conversely, high-aspect-ratio formats such as the 18 650 and 21 700 benefit more from SC due to their larger heat-exchange area, but their performance still remains inferior to tab-based approaches, especially when spatial uniformity and gradient minimization are critical.

Taken together, these findings indicate that no single cylindrical cell geometry is universally optimal. Instead, the ideal aspect ratio must be selected in conjunction with the intended cooling configuration: tab-based strategies favor short, bulky cells, while surface-only strategies favor tall, slim cells—though the latter still struggle to match the thermal uniformity achievable with tab cooling. Therefore, cylindrical cell design should be co-optimized with the thermal management strategy rather than determined in isolation.

VI. Conclusion

This article has developed a new battery modeling framework for spatially resolved thermal dynamics based on the CSC approach and model component decomposition. The obtained library of models is well-suited for online thermal performance optimization, thanks to its ability to independently control the tab and SC channels of the battery. This framework has been presented for both cylindrical and pouch cells and thoroughly evaluated through various combinations of tab and SC cases under real-world vehicle driving profiles.

By using four states, the model accurately predicts the local thermal behavior, even under aggressive vehicle driving and cooling scenarios. The model with only one state, in particular, is both more accurate and computationally efficient than the widely utilized two-state TEC model, with a 28.7% reduction in computational time. Even as the number of states increases, it remains in the same computational order of magnitude as the TEC model, suggesting it could readily replace the TEC model in existing BMSs.

Closed-loop temperature control of cylindrical cells under different cooling scenarios demonstrated that exclusively cooling through the top and bottom tabs yields the lowest thermal gradients under various C-rates. Furthermore, the model's utility extends to the evaluation of cell geometry on thermal performance. Dimension-perturbation analysis showed that no single aspect ratio is universally optimal, and cylindrical cells should be co-designed with the intended cooling strategy rather than optimized in isolation.

Future work will focus on extending the thermal model to pack-level assemblies. Beyond batteries, the versatile modeling framework can be extended to other systems governed by PDEs, making it a valuable tool across multiple engineering disciplines.

References

[1] S. Cevik, *Climate Change and Energy Security: The Dilemma or Opportunity of the Century*, Standard WP/22/123, 2022.

[2] S. Ma et al., "Temperature effect and thermal impact in lithium-ion batteries: A review," *Prog. Natural Science: Mater. Int.*, vol. 28, no. 6, pp. 653–666, Dec. 2018.

[3] J. Lin, X. Liu, S. Li, C. Zhang, and S. Yang, "A review on recent progress, challenges and perspective of battery thermal management system," *Int. J. Heat Mass Transf.*, vol. 167, Mar. 2021, Art. no. 120834.

[4] P. R. Tete, M. M. Gupta, and S. S. Joshi, "Developments in battery thermal management systems for electric vehicles: A technical review," *J. Energy Storage*, vol. 35, Mar. 2021, Art. no. 102255.

[5] Y. Zhao, L. B. Diaz, Y. Patel, T. Zhang, and G. J. Offer, "How to cool lithium ion batteries: Optimising cell design using a thermally coupled model," *J. Electrochemical Soc.*, vol. 166, no. 13, pp. A2849–A2859, 2019.

[6] I. A. Hunt, Y. Zhao, Y. Patel, and J. Offer, "Surface cooling causes accelerated degradation compared to tab cooling for lithium-ion pouch cells," *J. Electrochemical Soc.*, vol. 163, no. 9, pp. A1846–A1852, 2016.

[7] Y. Zhao, Y. Patel, T. Zhang, and G. J. Offer, "Modeling the effects of thermal gradients induced by tab and surface cooling on lithium ion cell performance," *J. Electrochemical Soc.*, vol. 165, no. 13, pp. A3169–A3178, 2018.

[8] O. Dondelewski et al., "The role of cell geometry when selecting tab or surface cooling to minimise cell degradation," *eTransportation*, vol. 5, Aug. 2020, Art. no. 100073.

[9] S. Li et al., "Optimal cell tab design and cooling strategy for cylindrical lithium-ion batteries," *J. Power Sources*, vol. 492, Apr. 2021, Art. no. 229594.

[10] C. Bolsinger and K. P. Birke, "Effect of different cooling configurations on thermal gradients inside cylindrical battery cells," *J. Energy Storage*, vol. 21, pp. 222–230, Feb. 2019.

[11] T. Ahmad, A. Mishra, S. Ghosh, and C. S. Casari, "Identifying efficient cooling approach of cylindrical lithium-IoN batteries," *Energy Technol.*, vol. 10, no. 2, Feb. 2022, Art. no. 2100888.

[12] G. K. Peprah, F. Liberati, F. Altaf, G. Osei-Dadzie, A. Di Giorgio, and A. Pietrabissa, "Optimal load sharing in reconfigurable battery systems using an improved model predictive control method," in *Proc. 29th Medit. Conf. Control Autom. (MED)*, Jun. 2021, pp. 979–984.

[13] X. Lin et al., "A lumped-parameter electro-thermal model for cylindrical batteries," *J. Power Sources*, vol. 257, pp. 1–11, Jul. 2014.

[14] V. Srinivasan and C. Y. Wang, "Analysis of electrochemical and thermal behavior of Li-ion cells," *J. Electrochemical Soc.*, vol. 150, no. 1, pp. A98–A106, Jan. 2003.

[15] J. Shen, T. Tang, and L.-L. Wang, *Spectral Methods: Algorithms, Analysis and Applications*, vol. 41. Cham, Switzerland: Springer, 2011.

[16] L. N. Trefethen, *Spectral Methods in MATLAB*. Philadelphia, PA, USA: SIAM, 2000.

[17] R. R. Richardson, S. Zhao, and D. A. Howey, "On-board monitoring of 2-D spatially-resolved temperatures in cylindrical lithium-ion batteries: Part I. low-order thermal modelling," *J. Power Sources*, vol. 326, pp. 377–388, Sep. 2016.

[18] X. Hu, W. Liu, X. Lin, Y. Xie, A. M. Foley, and L. Hu, "A control-oriented electrothermal model for pouch-type electric vehicle batteries," *IEEE Trans. Power Electron.*, vol. 36, no. 5, pp. 5530–5544, May 2021.

[19] D. W. Hahn and M. N. Özisik, *Heat Conduction*. Hoboken, NJ, USA: Wiley, 2012.

[20] T. G. Tranter, R. Timms, P. R. Shearing, and D. J. L. Brett, "Communication—Prediction of thermal issues for larger format 4680 cylindrical cells and their mitigation with enhanced current collection," *J. Electrochemical Soc.*, vol. 167, no. 16, Dec. 2020, Art. no. 160544.

[21] K.-J. Lee, G.-H. Kim, and K. Smith, "Three dimensional thermal and electrochemical model for spirally wound large format lithium-ion batteries," *ECS Meeting Abstr.*, vol. 2, no. 11, p. 1114, Jul. 2010.

[22] S. J. Farlow, *Partial Differential Equations for Scientists and Engineers*. New York, NY, USA: Dover, 1993.

[23] R. K. Nagle, E. B. Saff, A. D. Snider, and B. West, *Fundamentals of Differential Equations and Boundary Value Problems*. Reading, MA, USA: Addison-Wesley, 1996.
[24] E. H. Doha and A. H. Bhrawy, "An efficient direct solver for multidimensional elliptic Robin boundary value problems using a legendre spectral-Galerkin method," *Comput. Math. Appl.*, vol. 64, no. 4, pp. 558–571, Aug. 2012.
[25] F. Auteri, N. Parolini, and L. Quartapelle, "Essential imposition of Neumann condition in Galerkin–Legendre elliptic solvers," *J. Comput. Phys.*, vol. 185, no. 2, pp. 427–444, Mar. 2003.
[26] Y. Xie et al., "An improved resistance-based thermal model for a pouch lithium-ion battery considering heat generation of posts," *Appl. Thermal Eng.*, vol. 164, Jan. 2020, Art. no. 114455.
[27] X. Lin et al., "Online parameterization of lumped thermal dynamics in cylindrical lithium ion batteries for core temperature estimation and health monitoring," *IEEE Trans. Control Syst. Technol.*, vol. 21, no. 5, pp. 1745–1755, Sep. 2013.
[28] C. Zou, A. Klintberg, Z. Wei, B. Fridholm, T. Wik, and B. Egardt, "Power capability prediction for lithium-ion batteries using economic nonlinear model predictive control," *J. Power Sources*, vol. 396, pp. 580–589, Aug. 2018.
[29] V. Roscher et al., "Synchronisation using wireless trigger-broadcast for impedance spectroscopy of battery cells," in *Proc. IEEE Sensors Appl. Symp. (SAS)*, Apr. 2015, pp. 1–6.
[30] M. Fleckenstein, S. Fischer, O. Bohlen, and B. Bäker, "Thermal impedance spectroscopy–A method for the thermal characterization of high power battery cells," *J. Power Sources*, vol. 223, pp. 259–267, Feb. 2013.
[31] D. Bernardi, E. Pawlikowski, and J. Newman, "A general energy balance for battery systems," *J. Electrochemical Soc.*, vol. 132, no. 1, pp. 5–12, Jan. 1985.
[32] P. Mock, J. Kühlwein, U. Tietge, V. Franco, A. Bandivadekar, and J. German, "The WLTP: How a new test procedure for cars will affect fuel consumption values in the EU," *Int. Council Clean Transp.*, vol. 9, no. 3547, pp. 1–20, 2014.
[33] J. Li, J. Klee Barillas, C. Guenther, and M. A. Danzer, "A comparative study of state of charge estimation algorithms for LiFePO4 batteries used in electric vehicles," *J. Power Sources*, vol. 230, pp. 244–250, May 2013.
[34] C. Roe et al., "Immersion cooling for lithium-ion batteries—A review," *J. Power Sources*, vol. 525, Mar. 2022, Art. no. 231094.
[35] C. Multiphysics, "Introduction to comsol multiphysics," *COMSOL Multiphys.*, vol. 9, no. 2018, p. 32, 1998.

Godwin K. Peprah (Student Member, IEEE) received the B.Sc. degree in electrical and electronic engineering from the Kwame Nkrumah University of Science and Technology, Kumasi, Ghana, in 2014, the M.Sc. degree in control engineering from the La Sapienza University of Rome, Rome, Italy, in 2021, and the Licentiate of Engineering degree in systems and control from the Chalmers University of Technology, Gothenburg, Sweden, in 2024.

He was a Visiting Researcher with McMaster University, Hamilton, ON, Canada. His current research interests include advanced modeling, estimation, and automatic control of energy storage systems, with particular emphasis on battery thermal management.

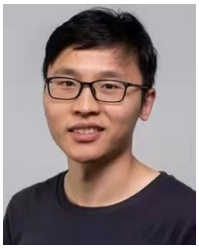

Yicun Huang received the M.Eng. degree in mechanical engineering from the University of Bristol, Bristol, U.K., in 2015, and the Ph.D. degree from the University of Canterbury, Christchurch, New Zealand, in 2020.

From 2021 to 2025, he was a Post-Doctoral Researcher and a Researcher with the Automatic Control Unit, Department of Electrical Engineering, Chalmers University of Technology, Gothenburg, Sweden. He is currently an Assistant Professor with the Division of Systems and Control, Department of Information Technology, Uppsala University, Uppsala, Sweden. His research focuses on advanced modeling for energy materials.

Dr. Huang was a recipient of the Marie Skłodowska-Curie Postdoctoral Fellowship in 2022 and received the Best Presentation Award from the 2022 International Conference on Energy and AI.

Torsten Wik (Member, IEEE) received the M.Sc. degree in chemical engineering, the Licentiate of Engineering degree in control engineering, and the Ph.D. and Docent degrees from the Chalmers University of Technology, Gothenburg, Sweden, in 1994, 1996, 1999, and 2004.

From 2005 to 2007, he worked as a Senior Researcher at Volvo Technology, Gothenburg, in control system design. In 2007, he was an Associate Professor with Chalmers University of Technology, where he is currently a Full Professor and the Head of Automatic Control at the Department of Electrical Engineering. His main research areas are optimal control, process control, and environmentally motivated control applications. During the last dozen years, the applications have increasingly been focused on battery management systems.

Faisal Altaf received the B.Sc. degree in mechatronics engineering from the National University of Sciences and Technology, Islamabad, Pakistan, in 2004, the M.Sc. degree in electrical engineering from the KTH Royal Institute of Technology, Stockholm, Sweden, in 2011, and the Ph.D. degree in control systems from the Chalmers University of Technology, Gothenburg, Sweden, in 2016.

He is currently the Senior Engineering Manager with the Energy Platform Department, Jaguar Land Rover, Warwick, U.K., where he leads a large Research and Development team developing advanced battery management system (BMS) solutions in-house for a wide range of electrified vehicles. With over two decades of experience in mechatronic system design, his core expertise spans batteries, model-based system engineering, controls, data analytics, and electronics. Over the past 15 years, his work has focused on battery performance and lifetime optimization while ensuring safety through advanced controls and battery intelligence for automotive and stationary energy storage applications. He has collaborated with the leading battery manufacturers, academic research groups, industrial partners, and innovative startups. Previously, he was the Chief Engineer at the Volvo Group, Gothenburg, and held several senior Research and Development roles in both industry and academia. He has published numerous research articles and holds several industrial patents in advanced BMS technologies.

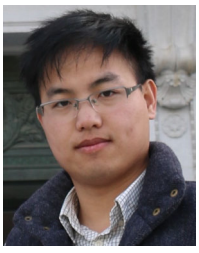

Changfu Zou (Senior Member, IEEE) received the Ph.D. degree in automation and control engineering from the University of Melbourne, Melbourne, VIC, Australia, in 2017.

He was a Visiting Student Researcher with the University of California, Berkeley, Berkeley, CA, USA, from 2015 to 2016. Since early 2017, he has been with the Automatic Control Unit, Department of Electrical Engineering, Chalmers University of Technology, Gothenburg, Sweden, where he is currently a Professor. His research interests include advanced modeling, monitoring, and automatic control of energy systems, particularly batteries.

Dr. Zou has secured competitive research funding from European Commission and Swedish National Agencies and has supervised six Marie Skłodowska-Curie Fellows. He was a recipient of multiple awards, including the IEEE Vehicular Technology Society Best Vehicular Electronics Paper Award and the IEEE Transactions on Transportation Electrification Prize Paper Award. He serves as an Associate Editor for journals, such as IEEE TRANSACTIONS ON VEHICULAR TECHNOLOGY, *IEEE Vehicular Technology Magazine*, and IEEE TRANSACTIONS ON TRANSPORTATION ELECTRIFICATION.